

Article

Breakup Dynamics of Semi-dilute Polymer Solutions in a Microfluidic Flow-focusing Device

Chun-Dong Xue ^{1,†}, Xiao-Dong Chen ^{2,†}, Yong-Jiang Li ¹, Guo-Qing Hu ³, Tun Cao ^{1,*} and Kai-Rong Qin ^{1,*}

¹ School of Optoelectronic Engineering and Instrumentation Science, Dalian University of Technology, Dalian 116024, China; xuechundong@dlut.edu.cn (C.-D.X.); yongjiangli@dlut.edu.cn (Y.-J.L.)

² School of Aerospace Engineering, Beijing Institute of Technology, Beijing 100081, China; xiaodong.chen@bit.edu.cn

³ Department of Engineering Mechanics, Zhejiang University, Hangzhou 310027, China; ghu@zju.edu.cn

* Correspondence: caotun1806@dlut.edu.cn (T.C.); krqin@dlut.edu.cn (K.-R.Q.)

† These authors contributed equally to this work.

Received: 14 March 2020; Accepted: 12 April 2020; Published: 14 April 2020



Abstract: Droplet microfluidics involving non-Newtonian fluids is of great importance in both fundamental mechanisms and practical applications. In the present study, breakup dynamics in droplet generation of semi-dilute polymer solutions in a microfluidic flow-focusing device were experimentally investigated. We found that the filament thinning experiences a transition from a flow-driven to a capillary-driven regime, analogous to that of purely elastic fluids, while the highly elevated viscosity and complex network structures in the semi-dilute polymer solutions induce the breakup stages with a smaller power-law exponent and extensional relaxation time. It is elucidated that the elevated viscosity of the semi-dilute solution decelerates filament thinning in the flow-driven regime and the incomplete stretch of polymer molecules results in the smaller extensional relaxation time in the capillary-driven regime. These results extend the understanding of breakup dynamics in droplet generation of non-Newtonian fluids and provide guidance for microfluidic synthesis applications involving dense polymeric fluids.

Keywords: droplet microfluidics; breakup dynamics; filament thinning; non-Newtonian fluids; flow-focusing device; extensional flow; semi-dilute polymer solutions

1. Introduction

Droplet microfluidics has been one of the fastest growing areas of microfluidics in the past two decades, with far-reaching applications [1–6]. Microdroplets provide isolated micro-scale compartments for versatile functions in chemical, biological, medical, and material sciences [1–4,7–12]. Precise control of droplet size is a prerequisite to establish a uniform microenvironment, to ensure homogeneous composition, and to deliver accurate dosing of a drug or chemical reactants in these scenarios [9,10,13]. As non-Newtonian fluids are ubiquitous in nature and industry, non-Newtonian droplets are frequently encountered in practical processes including pharmaceutical synthesis, cell encapsulation, drug screening and delivery [14–16]. Understanding of non-Newtonian droplet generation is imperative in both fundamental mechanisms and practical applications.

Polymer solutions often exhibit non-Newtonian properties, i.e., elasticity, shear-thinning, or both. They have been frequently used as the model media in the laboratory due to their facile accessibility and easy-to-adjust rheology. Previous studies have demonstrated that a small amount of polymer added to a Newtonian fluid markedly affects the fluid rheology and, successively, the dynamics of breakup of the fluid threads in macroscopic experiments [17–19]. This kind of breakup can be observed

in the experiments of capillary breakup extensional rheometry (CaBER), which has been developed as a novel method for rheology measurements of complex fluids [20–22]. Differing from the quiescent outer phase of free surface flows, the continuous phase fluid in droplet-based microfluidic devices deforms the interface of the two immiscible liquids and promotes interfacial instabilities [23–25]. Microfluidic devices with flow-focusing configuration are commonly used to generate microdroplets [23,26]. Typically, two immiscible liquids flow coaxially into separate channels with the continuous fluid flowing on both sides of the dispersed fluid, after which the resulting elongation-dominated flow field in the continuous liquid drives the dispersed liquid into a thin filament that breaks into separated droplets. The generation process becomes complicated when the dispersed phase is a non-Newtonian fluid, in which the delicate balance of capillary, inertial and viscous forces is influenced by extra factors such as the elastic stress [27–29].

The breakup dynamics of viscoelastic droplet generation in flow-focusing microchannels has been experimentally investigated by several groups. Blended with a small quantity of linear polymers, e.g., polyethylene oxide (PEO), pure water can become a viscoelastic fluid without shear-thinning. On the whole, the breakup dynamics of the elastic filament can be divided into a flow-driven regime and a capillary-driven regime based on transition time [30,31]. Initially, the thread head advances and restricts the flow of continuous fluid, resulting in an increase of the hydrostatic pressure upstream [32]. The increased pressure mainly triggers a fast necking of filament, forming the flow-driven regime in which the minimum thread width scales with the remaining time as a power-law relation [30,33,34]. The distribution of the accumulated pressure upstream then changes as the filament extends. The necking force decreases while the stretching force increases. Polymers in the dispersed thread are highly stretched while the elastic force starts to dominate and the necking enters into the later capillary-driven regime [31,35]. At the later stage, the thread thinning shows an exponential decay over time [30,31,33–36]. The exponential decay allows measurements of both the extensional relaxation time and the steady extensional viscosity [31,33,35]. In addition, the molecular weights of polymer and the dimensions of the microchannel have been reported to impose effects on the dynamics of filament breakup [31–33,35,37].

It is noted that most of the existing studies consider dilute polymer solutions, while more concentrated polymer solutions are frequently encountered in practical applications [5,14–16], which often exhibit non-Newtonian properties more than elasticity. Although several studies have also examined the effect of shear-thinning on filament breakup [38,39], the breakup behavior of dense polymer solutions exhibiting both elasticity and shear-thinning has rarely been addressed in microfluidic devices. In the present study, the breakup dynamics of semi-dilute polymer solutions in a flow-focusing microchannel are highlighted. The breakup morphology of semi-dilute PEO solutions is first characterized by comparing with those of the dilute and Newtonian counterparts. Filament thinning is then quantified by tracking the evolution of the minimum thread width, by which the flow-driven and capillary-driven regimes are identified. The characteristics in the breakup of the semi-dilute solutions are finally clarified by analyzing the two regimes in detail.

2. Materials and Methods

2.1. Fluids

The continuous and dispersed phase fluids were the olive oil and the aqueous solution of PEO (Sigma-Aldrich, Shanghai, China), respectively. The molecular weight of PEO was $M_w = 2 \text{ M}\cdot\text{Da}$. PEO solutions were prepared by adding PEO powders in deionized water (Milli-Q, 18 M Ω -cm) and blending it sufficiently using a shaker with a rate of 60/min for 1–2 days. Unlike previous studies focusing on dilute regimes, i.e., $c/c^* < 1$, semi-dilute solutions were focused on in this study, i.e., $c/c^* = 2.5\text{--}10$. The dilute cases, i.e., $c/c^* = 0.1\text{--}1$, were also considered for comparison. Here, c^* is the overlap concentration calculated as $c^* = 3M_w/4\pi R_g^3 N_A = 1000 \text{ ppm}$ (parts per million), where N_A is the Avogadro constant and $R_g = 0.02M_w^{0.58} = 90 \text{ nm}$ is the gyration radius of a single polymer

molecule [40]. The density (ρ_c) and viscosity (η_c) of olive oil were 0.92 g/cm^3 and $78 \text{ mPa}\cdot\text{s}$, respectively. The interfacial tension (σ) of the continuous and droplet phase was measured as $20.3 \pm 0.08 \text{ mN/m}$ using the pendant droplet method (Theta, Attension Inc., Goteborg, Switzerland).

2.2. Rheological Characterization

The rheological properties of PEO solutions were measured using a rotational rheometer with cone-plate (50 mm, 0.3 rad) (Physica MCR302, Anton Paar GmbH, Graz, Austria). The viscosities η were measured at shear rates of $0.1\text{--}3000 \text{ s}^{-1}$ (Figure 1a), and the complex moduli (G^*) as a function of angular frequency (ω) was measured in dynamic oscillatory experiments with a constant strain of 4% (Figure 1b). All the measurements were conducted at $25 \text{ }^\circ\text{C}$ maintained by a Peltier stage. The shear-rate-dependent viscosities and the complex moduli indicate the coexistence of shear-thinning and elasticity. Meanwhile, both the shear-thinning and the elasticity enhance with the PEO concentration c .

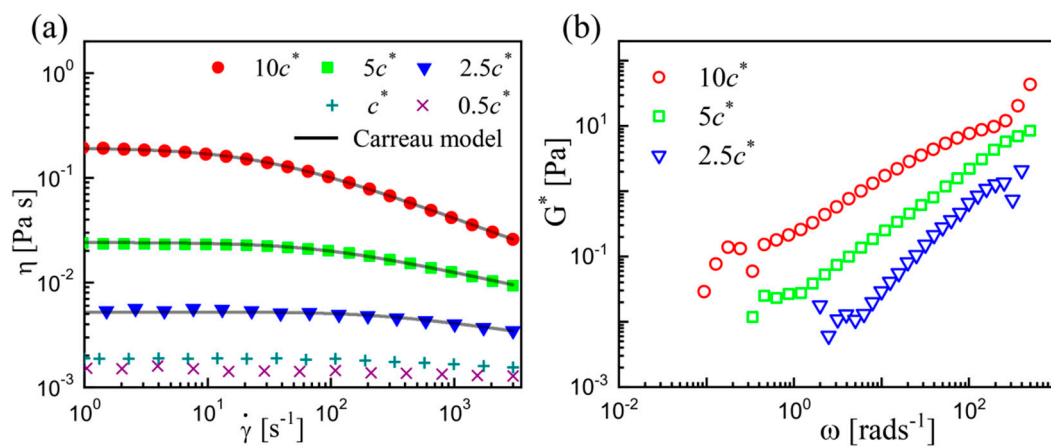


Figure 1. Rheological characterization of PEO solutions. (a) The measured viscosities η as a function of shear rate $\dot{\gamma}$ at different concentrations. The solid curves at $c > c^*$ are fitted by the modified Carreau model. The overlap concentration is $c^* = 1000 \text{ ppm}$. (b) The measured complex moduli at different concentrations.

To quantify the rheological properties of the semi-dilute solutions, a modified Carreau model [41,42] was used to fit the measured data:

$$\eta(\dot{\gamma}) = \eta_0 [1 + (\lambda_C \cdot \dot{\gamma})^a]^{(-d)/a} \quad (1)$$

where η_0 is the zero shear viscosity, λ_C is the characteristic time for the fluid, d is the negative of the power-law slope, and a is the fitting parameter introduced by Yasuda et al. [41] Note that the η_0 is viscosity at $\dot{\gamma} \sim O(10^{-1})$ in the actual measurement. Here, $d = 0$ signifies no shear-thinning. The d -value increases as PEO concentration increases, indicating the increased shear-thinning effect. The characteristic time λ_C corresponds to the critical shear rate ($\dot{\gamma}$) at which the η begins to decrease [41], which can be deemed as the relaxation time of the polymeric fluid in our measurements. All the fitting parameters are listed in Table 1.

Table 1. The fitting parameters of the Carreau model and three kinds of relaxation time for comparison.

c/c^*	$\eta_0 \text{ (mPa s)}$	d	a	$\lambda_C \text{ (ms)}$	$\lambda_R \text{ (ms)}$	$\lambda_1 \text{ (ms)}$	$\lambda_2 \text{ (ms)}$
2.5	5.2	0.16	1.3	4.2	5.2	-	9
5	24	0.25	1.1	12	15	19.4	12
10	193	0.43	0.96	35	42	86	26

For comparison, values for Zimm relaxation time (λ_Z) and reptation time (λ_R) are provided. The Zimm relaxation time is calculated based on the Zimm model [33,43,44], which can describe the relaxation of dilute solutions well. The λ_Z values were estimated by

$$\lambda_Z = 0.463 \frac{[\eta]M_w\eta_s}{N_A k_B T} \quad (2)$$

where $[\eta] = 0.072M_w^{0.65}$ is the intrinsic viscosity of PEO solution, η_s is the solvent viscosity, N_A is the Avogadro's number, k_B is the Boltzmann's constant, and T is the absolute temperature. The prefactor 0.463 accounts for the solvent quality and the excluded volume parameter. Accordingly, $\lambda_Z = 0.35$ ms is obtained, independent of the polymer concentrations. In contrast, the reptation model takes the hydrodynamic interactions into account and can better depict the polymer dynamics in semi-dilute solutions [45–47]. The λ_R value shows a concentration dependence, i.e.,

$$\lambda_R = \tau_0 N^3 / N_e(1) c^{3(1-v)/(3v-1)} \quad (3)$$

where $\tau_0 \approx 0.2$ ns is the monomer relaxation time at room temperature, $N = M_w/M_0$ is the number of Kuhn monomers per chain ($M_0 = 140$ for PEO), $N_e(1) \approx 14$ is the number of Kuhn monomers in an entanglement strand in melts, and $v = 0.588$ is the solvent quality exponent. The estimated λ_R values agree well with the values of λ_C for the semi-dilute solutions, as shown in Table 1. The estimated values of λ_C were also compared with those measured by other approaches, i.e., CaBER (λ_1) [21] and Dripping-onto-Substrate rheometry (DoSR) (λ_2) [44]. The comparison suggests that our estimated relaxation time values accord with those reported in these works (Table 1).

2.3. Experimental Setup

The flow-focusing configuration was employed in the present study, as shown in Figure 2. The main channel was 50 μm in both width and height (W_c). All the openings of the cross-slot structure were 50 μm . The intermediate inlet was set to introduce dispersed phase fluid. The two identical side openings are for continuous phases, which are then merged into one main inlet for easy control in actual operation. The chip was fabricated in polydimethylsiloxane (PDMS), based on the standard soft-lithography technique as described previously [48,49]. Before the experiments, the chips were kept in an oven at 80 $^\circ\text{C}$ overnight to restore the material to its native hydrophobic condition. The square geometry and the hydrophobic properties were designed to minimize the three-dimensional effect as far as possible, allowing us to rationally analyze the droplet generation process just from the in-plane images [35].

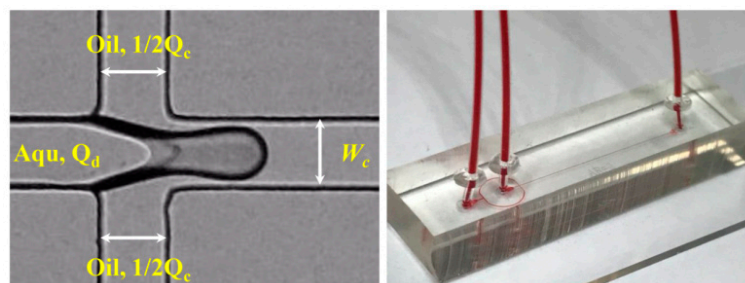


Figure 2. Channel configuration and assembled microchip. All the openings of the cross-slot channel are 50 μm . Q_c and Q_d represent the flow rates of the continuous phase and dispersed phase, respectively. Red ink was infused to visualize the channel structure in the assembled chip.

The experiments were performed under an inverted microscope (Nikon Eclipse Ti, Nikon Instruments Inc., Tokyo, Japan). The fluids were introduced into the assembled chip by two syringe pumps (Pump 11 Elite, Harvard apparatus Inc., Holliston, Massachusetts, United States) with two

1 mL plastic syringes (BD, Becton Dickinson Inc., Franklin lakes, New Jersey, United States). The flow rates of continuous and dispersed fluid were $Q_c = 20\text{--}160 \mu\text{L/h}$ and $Q_d = 1.25\text{--}160 \mu\text{L/h}$, respectively, and the flow rate ratios were $q = Q_c/Q_d = 1\text{--}16$. For this range of control parameters, the Reynolds number of continuous phase $Re_c = \rho_c W_c U_m / \eta_c$ is 0.001–0.01 and the capillary number $Ca_c = \eta_c U_m / \sigma$ is 0.009–0.07, where $U_m = Q_c / W_c^2$ is the average velocity of continuous phase fluid. The low Re_c and Ca_c indicate that in the quasi-static state the inertial forces are much smaller than the viscous forces and the viscous forces are much smaller than the surface forces. Moreover, to evaluate the importance of elasticity in the dispersed phase, the Weissenberg number, defined as the ratio between the fluid relaxation time and the flow characteristic time, was also considered. In the focused semi-dilute cases, $Wi = 2\lambda_Z Q_d / W_c^3 = 0.02\text{--}24.9$, suggesting that the elastic effect can dominate under most conditions.

The images of the droplet breakup process were recorded using a high-speed CCD camera (Phantom v7.3, Vision Research Inc., Birmingham, Alabama, United States) and the Phantom Camera Control software (PCC 2.14, Vision Research Inc., Birmingham, Alabama, United States). Experimental videos were taken at $10^3\text{--}10^4$ fps (frames per second). All of the experiments were conducted at the room temperature. The captured images were then processed and analyzed using the ImageJ software package (National Institute of Health, Bethesda, Maryland, USA). The maximum length error of image processing was estimated to be $4 \mu\text{m}$, and the time error was less than the interval between two successive images, i.e., $100 \mu\text{s}$.

3. Results and Discussion

3.1. Qualitative Observations

The image sequences listed in Figure 3 demonstrate the thinning processes of the dispersed thread for different polymer solutions under the identical flow condition, i.e., $q = 4$ and $Q_c = 40 \mu\text{L/h}$. The case of pure water, i.e., $c = 0$, exhibits typical filament thinning and droplet generation of Newtonian fluid. Initially, the dispersed thread starts to elongate and neck after it is driven into the junction. The thread then thins quickly and forms a primary droplet connected to a thin filament. The thin filament finally breaks into a satellite droplet. To simplify the analysis, the breakup time t_b is defined as the instant when the filament is uniform and the satellite droplets have not yet formed, as shown in Figure 3e. These observations are consistent with previous experiments [31,37,50].

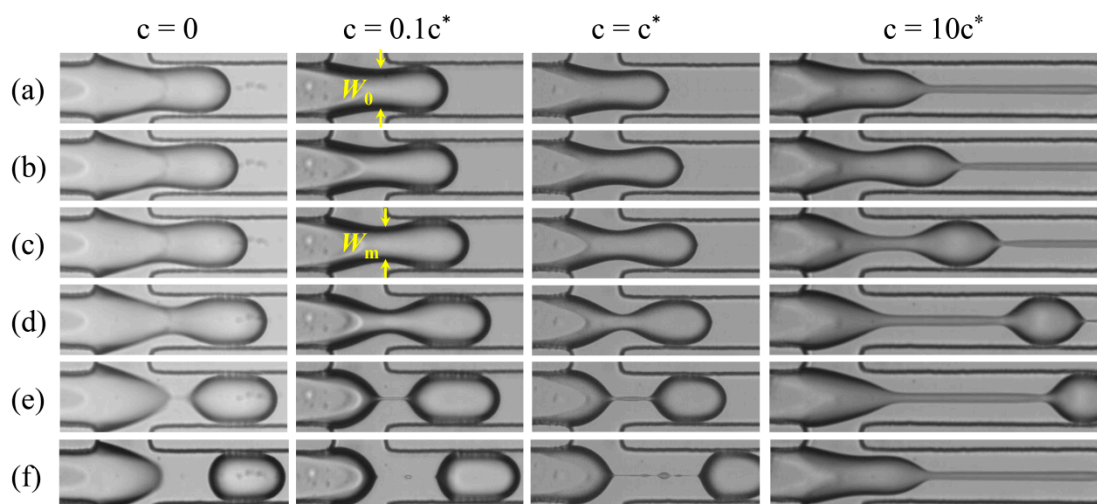


Figure 3. Sequences of images showing the thinning process of droplet generation for different solutions: (a) Initial regime; (b) $t/t_b = 0.2$; (c) $t/t_b = 0.4$; (d) $t/t_b = 0.8$; (e) $t/t_b = 1$; and (f) after breakup. Values of t_b for the four cases are 14.8, 16.8, 18.4 and 60 ms, respectively. W_0 represents the initial thread width and W_m represents the minimum thread width at a certain instant. For all cases, $q = 4$ and $Q_c = 40 \mu\text{L/h}$.

The polymeric cases exhibit different behavior at different polymer concentrations. The dilute solutions, i.e., $c = 0.1c^*$ and c^* , display behavior similar to the Newtonian counterpart. The dispersed fluid also develops into a thread that necks first and then breaks into a primary droplet and some tiny satellite droplets. The filament length and the breakup time in these polymeric cases are longer than those of the Newtonian counterpart, as previously reported [31,33]. Due to the low flow rate ratio q , the discrepancies here are not so large. Meanwhile, for the semi-dilute solution, i.e., $c = 10c^*$, the thread thinning exhibits a very different behavior. During the early phase, the morphology is similar to that of the Newtonian counterpart. As time elapses, the filament further elongates but thins at a much lower rate. The filament elongation and breakup time t_b are much longer. After breakup, the filament destabilizes and its width becomes non-uniform, leading to the well-known bead-on-a-string that forms multiple satellite droplets successively [31,51]. This process occurs between two primary droplets downstream and is not shown in the image. Although the satellite droplets formed during filament breakup, the primary droplets on which we focused in the current study are highly uniform for all cases. Notably, the satellite droplets become larger as the PEO concentration increases or the flow rate of continuous phase increases, inevitably reducing the uniformity of the generated droplets. How to improve the uniformity of polymeric droplets is another issue that deserves to be addressed in the future.

3.2. Quantitative Characterization

The observations above give us an intuitive impression. To capture more details, the process of filament thinning was quantitatively characterized by tracking the evolution of minimum width of filament W_m . The distinct interface of dispersed thread offers the chance to track the evolution of filament width. As denoted in Figure 3, the width at the instant when the thread starts to form is defined as the initial width W_0 , and this instant is defined as the initial time $t = 0$. As time elapses, the thread deforms to form a necked filament. The distance between the two points with zero curvature in the neck is defined as the minimum width of filament W_m . As the thinning progresses, the measurement location of W_m shifts slightly but always maintains a location near the cross-slot. The time evolution of W_m is then extracted from the sequential images of individual thinning period. To ensure reliability, more than three measurements were carried out for each case.

Figure 4 shows the typical results of time-varied W_m under different conditions. The measured data are truncated at the breakup time t_b when the width thread is uniform, and the satellite droplets have not formed yet. The result of pure water ($c = 0$) is provided as the Newtonian counterpart. As shown by the black solid curve in Figure 4, the power-law fit $W_m \sim (14.8 - t)^{0.32}$ is consistent with previous microscopic experiments with Newtonian fluids [37,50]. In contrast, the polymeric cases display a different behavior. The decay is similar to that of the Newtonian counterpart in the early stages but deviates upwards later. The deviation enhances with the increasing concentration c , and the breakup time t_b increases. Moreover, the retardation of decay in the early stage can be noticed when the polymer concentration c increases to the semi-dilute regime ($c > c^*$). This retardation also shows a positive dependence on the polymer concentration c . This will be further explained in combination with the fitting law in the next section.

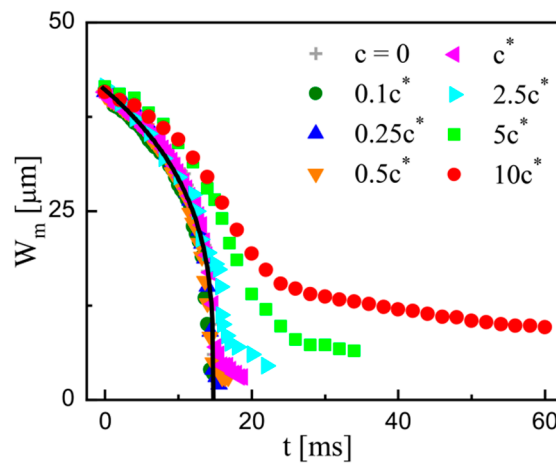


Figure 4. Time evolution of the minimum filament width W_m at different PEO concentrations. The black solid curve $W_m \sim (14.8 - t)^{0.32}$ is the fit for the Newtonian case, i.e., $c = 0$. The flow conditions are identical.

The instant when the deviation starts can be defined as the transition time t_p . For the viscoelastic filament, the thinning process is divided into a flow-driven stage and an elasto-capillary stage based on the transition time t_p [30,31], which can be captured by comparing the time-varied profiles of W_m between the polymeric fluid and the Newtonian counterpart [30,43]. As shown in Figure 4, it is valid for dilute solutions ($c \leq c^*$) but cannot be directly applied for semi-dilute solutions ($c > c^*$) in the current study. Here, we propose a method to extract the values of t_p based on the temporal variation of the extensional strain rates in the filament thinning. The extensional strain rates can be calculated by [30,31,43,52]

$$\dot{\epsilon} = \frac{-2}{W_m} \frac{dW_m}{dt} \tag{4}$$

It is found that the values of $\dot{\epsilon}$ increase initially and decrease afterwards as time elapses, and the two-staged characteristics are generic for all the examined solutions (Figure 5a). The moment when the maximum $\dot{\epsilon}$ occurs can be reasonably regarded as the transition time t_p , before which the elastic stress is negligible. The elastic stress becomes dominant only when the polymer molecules are stretched to a certain extent at the maximum $\dot{\epsilon}$ [31,43].

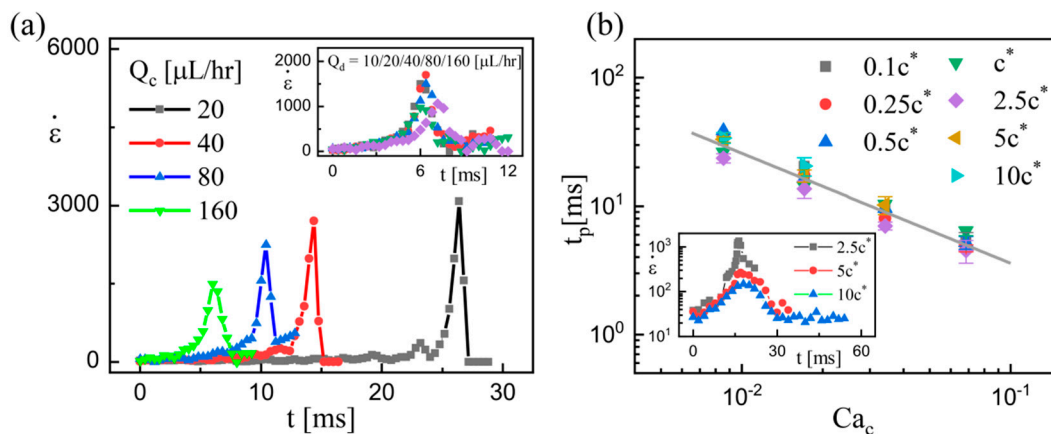


Figure 5. (a) Extensional strain rate $\dot{\epsilon}$ as functions of the elapsed time at different Q_c . The moment when the maximum $\dot{\epsilon}$ occurs is regarded as the transition time t_p . The PEO concentration $c = c^*$. Inset: The time-varied $\dot{\epsilon}$ at different Q_d . (b) Values of transition time t_p as functions of capillary number Ca_c . The straight line $t_p \sim Ca_c^{-0.86}$ is the best fit, and the error bars represent standard deviations. Inset: The time-varied $\dot{\epsilon}$ at different c .

Figure 5a shows the extensional strain rate $\dot{\epsilon}$ as a function of the elapsed time at different flow rates of continuous phase Q_c , and the variation of $\dot{\epsilon}$ at various flow rates of dispersed phase Q_d (inset). It is clear that the transition time t_p inversely depends on Q_c but is almost independent of Q_d . Conceivably, the increasing Q_c can accelerate the rate of droplet generation, in which the required time for individual filament thinning decreases. The transition time t_p decreases as a consequence. In contrast, the increasing Q_d always enhances the droplet size but hardly affects the generation rate, thus imposing a negligible effect on t_p . In addition, although the time evolution curves of W_m at different PEO concentrations are different (Figure 4), the transition time t_p varies slightly as the PEO concentration increases (inset in Figure 5b). By analyzing all the experimentally captured values of t_p , the relation of Q_c and t_p can be established, as shown in Figure 5b. The dimensionless parameter Ca_c (proportional to Q_c) is introduced to fit the relation $t_p \sim Ca_c^{-0.86}$.

It is obvious that the filament thinning can be divided into two regimes based on the transition time t_p for all the examined PEO solutions (Figure 4). This two-stage feature is the same to the previous experiments for purely elastic fluids, in which a power-law function along with an exponential function are often used to fit the thinning process [30,33,43,44,53]. It is widely acknowledged that the power-law function characterizes the flow-driven regime, while the exponential function characterizes the capillary-driven regime in the viscoelastic cases. Here, a combination of the two functions is also tried to fit our measured data for the semi-dilute solutions. Figure 6 shows the typical fitting of the time-varied profile of W_m at $c = 2.5c^*$, in which $W_m \sim (t_p - t)^{0.24}$ and $W_m \sim \exp[-0.39(t - t_p)]$ are separately denoted by the solid and dotted curves. For a denser solution ($c = 10c^*$), the similar fit can be obtained (see inset in Figure 6). These results demonstrate that the combination of flow-driven regime and capillary-driven regime is applicable for all the examined PEO solutions. To unveil the potential effects of the other properties in semi-dilute polymer solutions, the two regimes are separately analyzed in detail.

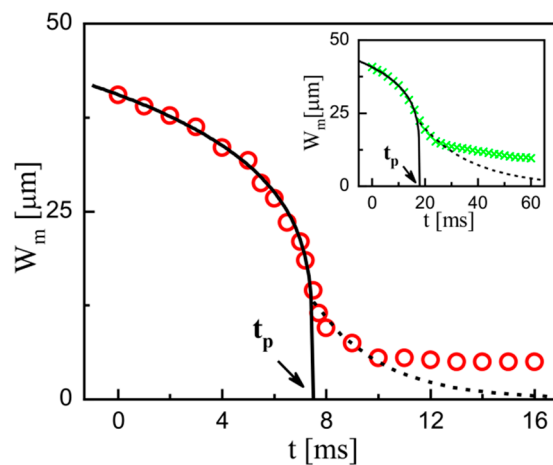


Figure 6. Typical fitting of the time-varied W_m at $c = 2.5c^*$. The flow conditions are $q = 8$ and $Q_c = 80 \mu\text{L/h}$. The fitting is a combination of $W_m \sim (t_p - t)^\alpha$ ($\alpha = 0.24$, solid curve) and $W_m \sim \exp[-\kappa(t - t_p)]$ ($\kappa = 0.39$, dotted curve). The transition time t_p and breakup time t_b are 7.5 ms and 16 ms, respectively. Inset: The experimental data at $c = 10c^*$ and the corresponding fit. The flow conditions are $q = 4$ and $Q_c = 40 \mu\text{L/h}$. t_p and t_b are 18 ms and 60 ms, respectively. The fitting parameters are $\alpha = 0.21$ and $\beta = 0.048$.

3.3. Flow-Driven Regime

To describe the relation of the minimum filament width W_m to the remaining time $(t_p - t)$ in the flow-driven regime, a power-law function was applied as follows:

$$W_m/W_c = A [(t_p - t)/\tau_T]^\alpha \tag{5}$$

where W_c is the channel width and $\tau_T = \eta_d W_c / \sigma$ is the characteristic viscous time, and they are used to build the dimensionless quantity. Figure 7 shows the experimental data and the corresponding fits. Parameter A also shows a positive dependence on the flow rate of continuous phase and the viscosity of dispersed phase at $c \geq c^*$, i.e., $A = 0.36Ca_c^{0.13}$ and $A = 1.36Ca_d^{0.33}$, where $Ca_d = Ca_c(\eta_c/\eta_d)$, consistent with those in the Newtonian and dilute cases [30,50]. At a fixed concentration of $c = 2.5c^*$, a power-law exponent $\alpha = 0.25 \pm 0.02$ is obtained, independent of the flow rate ratio q and the flow rate of continuous phase Q_c (Figure 7a). The constant exponent indicates a self-similar breakup process in the flow-driven regime in current configuration. The exponent α is approximately 1/4 and is smaller to the 2/3 or 1/2 for free liquid threads [43,44,54], reflecting the effects of the channel confinement and external flow. Moreover, the exponent α shows a dependence on the PEO concentration c , as illustrated in Figure 7b. For the dilute solutions with $c \leq c^*$, the constant exponent $\alpha = 0.30 \pm 0.02$, which is in consistent with $\alpha = 0.36$, was obtained for the purely elastic fluids in the similar flow-focusing microchannel [30]. At the highest concentration of $c = 10c^*$, the exponent $\alpha = 0.20 \pm 0.02$. Meanwhile, the exponent α decreases with the increasing c in the semi-dilute cases ($c > c^*$).

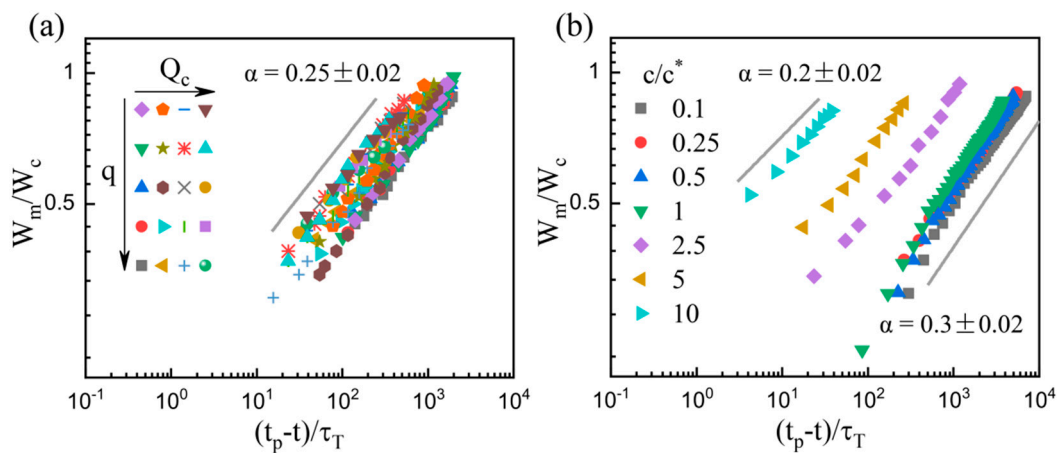


Figure 7. Plots of the dimensionless minimum width W_m/W_c of the dispersed filament to the dimensionless remaining time $(t_p - t)/\tau_T$ for $c = 2.5c^*$ under different flow conditions (a) and for different concentrations (b). In (a), $q = 1-16$ and $Q_c = 20-160 \mu\text{L/h}$. In (b), $q = 2$ and $Q_c = 40 \mu\text{L/h}$. All grey lines are provided to guide the eye.

The decreased exponent α indicates the deceleration of filament thinning in the flow-driven regime, which is caused by the elevated viscosity of the dispersed thread. The rheological measurement shows that the viscosity of polymer solution increases with increasing c (Figure 1a). In dilute cases, the increment is very limited, i.e., the viscosity at $c = c^*$ is only two times that of pure water. As c further increases, a dramatic increase occurs, e.g., the viscosity at $c = 10c^*$ is greater than that of pure water by two orders of magnitude (Table 1). The highly elevated viscosity of the dispersed thread in semi-dilute cases consequentially inhibits filament thinning. Besides, the bulk rheology also shows that the shear-thinning effect (reflected by d -value) enhances with increasing c (Table 1). In contrast to the effect of elevated viscosity, shear-thinning should exert an effect to accelerate the breakup (by improving the exponent α). However, our results report the decreased exponent α , suggesting the screened effect of shear-thinning in the current experiments, which agrees with the observations of previous experiments for purely shear-thinning fluids [38,39].

3.4. Capillary-Driven Regime

In the capillary-driven regime with $t > t_p$, the relationship between dimensionless minimum filament width W_m/W_c to dimensionless remaining time $(t - t_p)/\tau_T$ can be depicted by an exponential function:

$$W_m/W_c \propto \exp[\kappa(t - t_p)/\tau_T] \tag{6}$$

Figure 8a shows the experimental data at various PEO concentrations, which suggests that the exponential decay is genetic in both dilute and semi-dilute cases. The results are also in line with those for purely elastic fluids in previous experiments [30,33,35,43]. Moreover, the values of parameter κ barely depend on the flow conditions, as demonstrated in Figure 8b. Recalling the previous theory, the exponential regime for high viscosity elastic fluids based on the balance between elastic and capillary forces follows the function [19,43,54]

$$W_m/W_c \propto \exp[-(t - t_p)/3\lambda_E] \tag{7}$$

where λ_E is the extensional relaxation time. The relation $\lambda_E = -\tau_T/(3\kappa)$ can be derived and the values of λ_E for all the examined solutions can be calculated. The latent distinction between dilute and semi-dilute cases could be acquired by the analysis of λ_E .

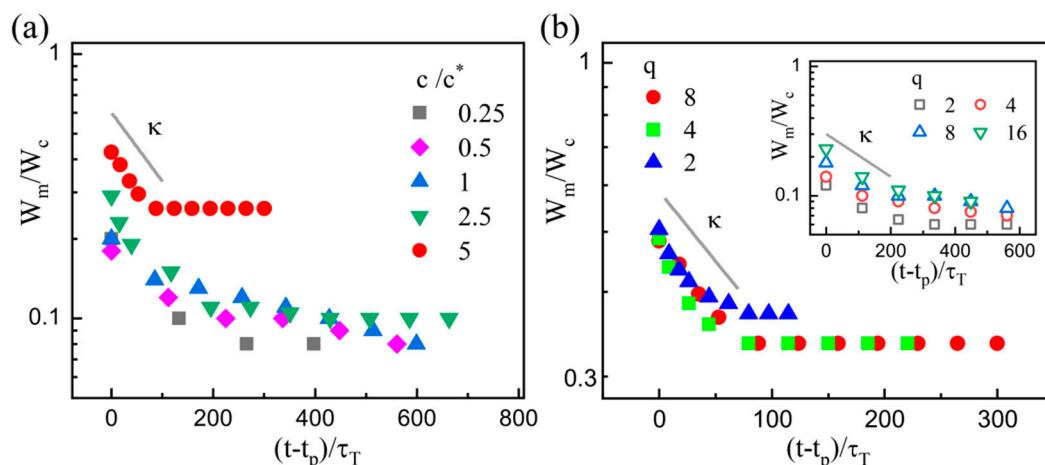


Figure 8. Plot of the dimensionless minimum width W_m/W_c of the dispersed filament to the dimensionless shifted time $(t - t_p)/\tau_T$ at (a) various c ; and (b) $c = 5c^*$. In (a), $q = 8$ and $Q_c = 80 \mu\text{L/h}$. In (b), $Q_c = 80 \mu\text{L/h}$. Inset: $c = 0.5c^*$ and $Q_d = 10 \mu\text{L/h}$.

Figure 9a shows the estimated values of extensional relaxation time λ_E for all the examined solutions. For the dilute solutions, i.e., $c \leq c^*$, the λ_E values are several times greater than the Zimm relaxation time λ_Z (dotted line in Figure 9a), which agrees with the findings of previous similar experiments [33]. Due to the microchannel confinements and the continuous phase flow, these estimated λ_E values are generally smaller than those captured in the pinch-off experiments of free surface fluid [33,43,44]. For the semi-dilute solutions, i.e., $c > c^*$, the estimated λ_E shows similar c -dependence ($\lambda_E \sim c^{1.6}$) with the reptation time λ_R ($\lambda_R \sim c^{1.5}$), while the λ_E values are obviously smaller than λ_R . These smaller λ_E values indicate the incomplete stretch of polymer molecules in the capillary-driven regime. This coincides with the result that the coil-stretch transition becomes milder for more concentrated polymer solutions in both macroscopic and microscopic extensional flows [44,55]. Moreover, the accumulated strain or Hencky strain ϵ can be calculated as $\epsilon = 2\ln(W_0/W_t)$, [35,52] where W_t denotes the time-varied W_m . It is thus found that the maximum strain $\epsilon_{\max} = [4.5-6]$ at $c = 0.1c^*$, while $\epsilon_{\max} = [1-2]$ at $c = 10c^*$. This contrast supports the claim of incomplete stretch in the semi-dilute solutions.

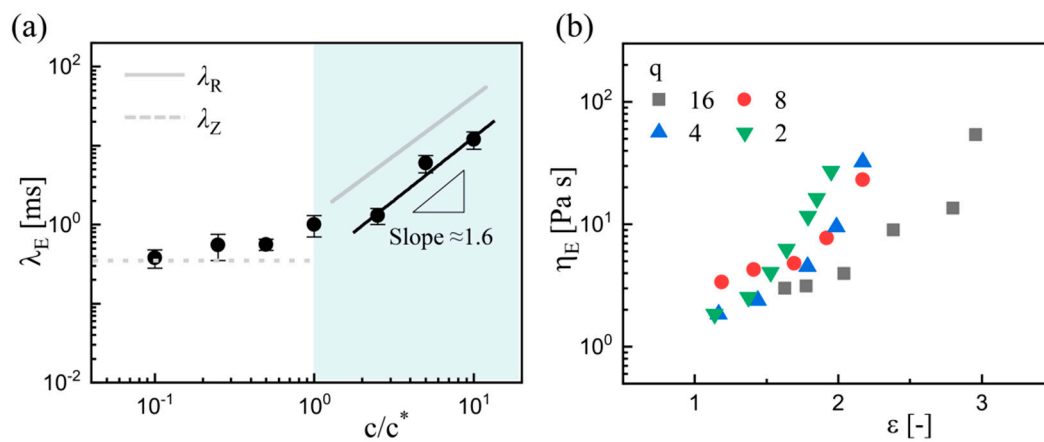


Figure 9. Results of extensional relaxation time λ_E and extensional viscosity η_E . (a) Variation of extensional relaxation time values λ_E with PEO concentrations. The grey line represents the predicted values for reptation time λ_R , and the grey dashed line represents the predicted values for the Zimm relaxation time λ_Z . (b) Evolution of extensional viscosity η_E with Hencky strain ϵ at $c = 5c^*$.

It is speculated that the incomplete stretch is due to the dense network structures in the semi-dilute solutions. According to the blob theory [45,47], each PEO molecule forms a blob when c is below c^* and all the blobs do not contact with each other. As c increases above c^* , blobs overlap with each other to form the networks and the network structures become denser with increasing polymer concentrations. For dilute polymer solutions, individual polymer blobs can be highly stretched in the filament. For semi-dilute polymer solutions, the networks are stretched as a whole and the individual polymer chains are just partially stretched, resulting in the lower strain ϵ , as stated above.

Furthermore, the extensional viscosity is introduced due to the polymer stretch. The extensional viscosity η_E is finally examined, which is calculated using the formula [30,44]

$$\eta_E = \frac{\sigma}{\dot{\epsilon}W_t} = \frac{\sigma}{-2dW_m/dt} \tag{8}$$

Figure 9b illustrates the variation of extensional viscosity η_E with an increasing Hencky strain ϵ at $c = 5c^*$. The extensional viscosity η_E increases with the strain ϵ , indicating the obvious strain hardening that has been reported in both macroscopic [53,54] and other microscopic experiments [30,31,33]. The absolute values of η_E are two to three orders of magnitude greater than their zero-shear viscosity η_0 , and this enhancement contributes to the delayed breakup. In the final stage, the filament further elongates and thins nearly linearly with time (Figures 4 and 6). The last regime allows the measurement of terminal steady extensional viscosity, which would be reached before all the chains are completely stretched out [44,56]. It is predicted that the final regime is maintained by the competitive effect between the continued stretch of the polymer chains and the drainage of the dispersed filament. This mechanism needs to be further validated by studying the polymer dynamics in the filament in the future work.

4. Conclusions

In summary, we experimentally investigate the filament breakup in droplet generation of semi-dilute PEO solutions in a flow-focusing microchannel. The breakup morphology of semi-dilute PEO solutions is analogous to that in dilute cases, which falls into a universal temporal profile in combination with a flow-driven regime and a capillary-driven regime. The transition time t_p dividing the two regimes is extracted based on the temporal variation of the extensional strain rates. The power-law exponent α characterizing the flow-driven regime in semi-dilute cases is smaller than that in dilute cases and decreases with increasing PEO concentration. It is ascertained that the highly elevated viscosity of the semi-dilute solution decelerates the filament thinning in the flow-driven

regime while the accelerating effect of shear-thinning is screened. The capillary-driven regime is analyzed based on the extensional relaxation time λ_E and the extensional viscosity η_E . The extensional relaxation time λ_E being less than the reptation time λ_R indicates the incomplete stretch of polymer molecules in the capillary-driven regime. The extensional viscosity η_E shows obvious strain hardening, and the significant enhancement of η_E contributes to the delayed breakup. These results extend the understanding of breakup dynamics in droplet generation of non-Newtonian fluids and could provide guidance for microfluidic synthesis applications involving semi-dilute polymer solutions.

Author Contributions: C.-D.X., X.-D.C. and K.-R.Q. conceived and designed the experiments; C.-D.X. and X.-D.C. performed the experiments and analyzed the data; Y.-J.L., G.-Q.H. and T.C. gave scientific support and conceptual advices; and C.-D.X. wrote the draft. All authors have read and agreed to the published version of the manuscript.

Funding: This research was funded by the National Natural Science Foundation of China (11802054, 11672065 and 11772343), the Fundamental Research Funds for the Central Universities (DUT19RC(4)032 and DUT19ZD201), and the China Postdoctoral Science Foundation (2019M651106).

Conflicts of Interest: The authors declare no conflict of interest.

References

1. Anna, S.L. Droplets and Bubbles in Microfluidic Devices. *Annu. Rev. Fluid Mech.* **2016**, *48*, 285–309. [[CrossRef](#)]
2. Mashaghi, S.; Abbaspourrad, A.; Weitz, D.A.; van Oijen, A.M. Droplet microfluidics: A tool for biology, chemistry and nanotechnology. *TrAC Trend. Anal. Chem.* **2016**, *82*, 118–125. [[CrossRef](#)]
3. Kaminski, T.S.; Scheler, O.; Garstecki, P. Droplet microfluidics for microbiology: Techniques, applications and challenges. *Lab Chip* **2016**, *16*, 2168–2187. [[CrossRef](#)] [[PubMed](#)]
4. Vecchiolla, D.; Giri, V.; Biswal, S.L. Bubble–bubble pinch-off in symmetric and asymmetric microfluidic expansion channels for ordered foam generation. *Soft Matter* **2018**, *14*, 9312–9325. [[CrossRef](#)]
5. Majumder, S.; Wubshet, N.; Liu, A.P. Encapsulation of complex solutions using droplet microfluidics towards the synthesis of artificial cells. *J. Micromech. Microeng.* **2019**, *29*, 083001. [[CrossRef](#)]
6. Ding, Y.; Howes, P.D.; DeMello, A.J. Recent Advances in Droplet Microfluidics. *Anal. Chem.* **2020**, *92*, 132–149. [[CrossRef](#)]
7. Shembekar, N.; Chaipan, C.; Utharala, R.; Merten, C.A. Droplet-based microfluidics in drug discovery, transcriptomics and high-throughput molecular genetics. *Lab Chip* **2016**, *16*, 1314–1331. [[CrossRef](#)]
8. Zhu, Z.; Yang, C.J. Hydrogel Droplet Microfluidics for High-Throughput Single Molecule/Cell Analysis. *Acc. Chem. Res.* **2017**, *50*, 22–31. [[CrossRef](#)]
9. Xu, Q.; Hashimoto, M.; Dang, T.T.; Hoare, T.; Kohane, D.S.; Whitesides, G.M.; Langer, R.; Anderson, D.G. Preparation of monodisperse biodegradable polymer microparticles using a microfluidic flow-focusing device for controlled drug delivery. *Small* **2009**, *5*, 1575–1581. [[CrossRef](#)]
10. Deng, X.; Ren, Y.; Hou, L.; Liu, W.; Jiang, T.; Jiang, H. Compound-Droplet-Pairs-Filled Hydrogel Microfiber for Electric-Field-Induced Selective Release. *Small* **2019**, e1903098. [[CrossRef](#)]
11. Liu, J.; Lan, Y.; Yu, Z.; Tan, C.S.; Parker, R.M.; Abell, C.; Scherman, O.A. Cucurbit[n]uril-Based Microcapsules Self-Assembled within Microfluidic Droplets: A Versatile Approach for Supramolecular Architectures and Materials. *Acc. Chem. Res.* **2017**, *50*, 208–217. [[CrossRef](#)] [[PubMed](#)]
12. Samal, P.; van Blitterswijk, C.; Truckenmüller, R.; Giselbrecht, S. Grow with the Flow: When Morphogenesis Meets Microfluidics. *Adv. Mater.* **2019**, *31*, 1805764. [[CrossRef](#)] [[PubMed](#)]
13. Taassob, A.; Manshadi, M.K.D.; Bordbar, A.; Kamali, R. Monodisperse non-Newtonian micro-droplet generation in a co-flow device. *J. Braz. Soc. Mech. Sci.* **2017**, *39*, 2013–2021. [[CrossRef](#)]
14. Abate, A.R.; Kutsovsky, M.; Seiffert, S.; Windbergs, M.; Pinto, L.F.; Rotem, A.; Utada, A.S.; Weitz, D.A. Synthesis of monodisperse microparticles from non-Newtonian polymer solutions with microfluidic devices. *Adv. Mater.* **2011**, *23*, 1757–1760. [[CrossRef](#)]
15. Lu, X.; Liu, C.; Hu, G.; Xuan, X. Particle manipulations in non-Newtonian microfluidics: A review. *J. Colloid Interface Sci.* **2017**, *500*, 182–201. [[CrossRef](#)]
16. Yuan, D.; Zhao, Q.; Yan, S.; Tang, S.Y.; Alici, G.; Zhang, J.; Li, W. Recent progress of particle migration in viscoelastic fluids. *Lab Chip* **2018**, *18*, 551–567. [[CrossRef](#)]

17. Wagner, C.; Amarouchene, Y.; Bonn, D.; Eggers, J. Droplet detachment and satellite bead formation in viscoelastic fluids. *Phys. Rev. Lett.* **2005**, *95*, 164504. [[CrossRef](#)]
18. Clasen, C.; Eggers, J.; Fontelos, M.A.; Li, J.I.E.; McKinley, G.H. The beads-on-string structure of viscoelastic threads. *J. Fluid Mech.* **2006**, *556*, 283. [[CrossRef](#)]
19. Anna, S.L.; McKinley, G.H. Elasto-capillary thinning and breakup of model elastic liquids. *J. Rheol.* **2001**, *45*, 115–138. [[CrossRef](#)]
20. Rodd, L.E.; Scott, T.P.; Cooper-White, J.J.; McKinley, G.H. Capillary Break-up Rheometry of Low-Viscosity Elastic Fluids. *Appl. Rheol.* **2005**, *15*, 12–27. [[CrossRef](#)]
21. Arnolds, O.; Buggisch, H.; Sachsenheimer, D.; Willenbacher, N. Capillary breakup extensional rheometry (CaBER) on semi-dilute and concentrated polyethyleneoxide (PEO) solutions. *Rheol. Acta* **2010**, *49*, 1207–1217. [[CrossRef](#)]
22. Del Giudice, F.; D'Avino, G.; Greco, F.; De Santo, I.; Netti, P.A.; Maffettone, P.L. Rheometry-on-a-chip: Measuring the relaxation time of a viscoelastic liquid through particle migration in microchannel flows. *Lab Chip* **2015**, *15*, 783–792. [[CrossRef](#)] [[PubMed](#)]
23. Christopher, G.F.; Anna, S.L. Microfluidic methods for generating continuous droplet streams. *J. Phys. D Appl. Phys.* **2007**, *40*, R319–R336. [[CrossRef](#)]
24. van Hoeve, W.; Dollet, B.; Versluis, M.; Lohse, D. Microbubble formation and pinch-off scaling exponent in flow-focusing devices. *Phys. Fluids* **2011**, *23*, 092001. [[CrossRef](#)]
25. Chen, X.; Xue, C.; Hu, G. Confinements regulate capillary instabilities of fluid threads. *J. Fluid Mech.* **2019**, *873*, 816–834. [[CrossRef](#)]
26. Carneiro, J.; Doutel, E.; Campos, J.B.L.M.; Miranda, J.M. PDMS droplet formation and characterization by hydrodynamic flow focusing technique in a PDMS square microchannel. *J. Micromech. Microeng.* **2016**, *26*, 105013. [[CrossRef](#)]
27. Derzsi, L.; Kasprzyk, M.; Plog, J.P.; Garstecki, P. Flow focusing with viscoelastic liquids. *Phys. Fluids* **2013**, *25*, 092001. [[CrossRef](#)]
28. Ren, Y.; Liu, Z.; Shum, H.C. Breakup dynamics and dripping-to-jetting transition in a Newtonian/shear-thinning multiphase microsystem. *Lab Chip* **2015**, *15*, 121–134. [[CrossRef](#)]
29. Dinic, J.; Sharma, V. Computational analysis of self-similar capillary-driven thinning and pinch-off dynamics during dripping using the volume-of-fluid method. *Phys. Fluids* **2019**, *31*, 021211. [[CrossRef](#)]
30. Du, W.; Fu, T.; Zhang, Q.; Zhu, C.; Ma, Y.; Li, H.Z. Breakup dynamics for droplet formation in a flow-focusing device: Rupture position of viscoelastic thread from matrix. *Chem. Eng. Sci.* **2016**, *153*, 255–269. [[CrossRef](#)]
31. Arratia, P.E.; Gollub, J.P.; Durian, D.J. Polymeric filament thinning and breakup in microchannels. *Phys. Rev. E Stat. Nonlin. Soft Matter Phys.* **2008**, *77*, 036309. [[CrossRef](#)] [[PubMed](#)]
32. Garstecki, P.; Stone, H.A.; Whitesides, G.M. Mechanism for flow-rate controlled breakup in confined geometries: A route to monodisperse emulsions. *Phys. Rev. Lett.* **2005**, *94*, 164501. [[CrossRef](#)] [[PubMed](#)]
33. Steinhaus, B.; Shen, A.Q.; Sureshkumar, R. Dynamics of viscoelastic fluid filaments in microfluidic devices. *Phys. Fluids* **2007**, *19*, 073103. [[CrossRef](#)]
34. Du, W.; Fu, T.; Zhang, Q.; Zhu, C.; Ma, Y.; Li, H.Z. Self-similar breakup of viscoelastic thread for droplet formation in flow-focusing devices. *AIChE J.* **2017**, *63*, 5196–5206. [[CrossRef](#)]
35. Arratia, P.E.; Cramer, L.A.; Gollub, J.P.; Durian, D.J. The effects of polymer molecular weight on filament thinning and drop breakup in microchannels. *New J. Phys.* **2009**, *11*, 115006. [[CrossRef](#)]
36. Lee, W.; Walker, L.M.; Anna, S.L. Competition Between Viscoelasticity and Surfactant Dynamics in Flow Focusing Microfluidics. *Macromol. Mater. Eng.* **2011**, *296*, 203–213. [[CrossRef](#)]
37. Dollet, B.; van Hoeve, W.; Raven, J.P.; Marmottant, P.; Versluis, M. Role of the channel geometry on the bubble pinch-off in flow-focusing devices. *Phys. Rev. Lett.* **2008**, *100*, 034504. [[CrossRef](#)]
38. Aytouna, M.; Paredes, J.; Shahidzadeh-Bonn, N.; Moulinet, S.; Wagner, C.; Amarouchene, Y.; Eggers, J.; Bonn, D. Drop formation in non-Newtonian fluids. *Phys. Rev. Lett.* **2013**, *110*, 034501. [[CrossRef](#)]
39. Du, W.; Fu, T.; Duan, Y.; Zhu, C.; Ma, Y.; Li, H.Z. Breakup dynamics for droplet formation in shear-thinning fluids in a flow-focusing device. *Chem. Eng. Sci.* **2018**, *176*, 66–76. [[CrossRef](#)]
40. Xue, C.; Zheng, X.; Chen, K.; Tian, Y.; Hu, G. Probing Non-Gaussianity in Confined Diffusion of Nanoparticles. *J. Phys. Chem. Lett.* **2016**, *7*, 514–519. [[CrossRef](#)]
41. Yasuda, K.; Armstrong, R.C.; Cohen, R.E. Shear flow properties of concentrated solutions of linear and star branched polystyrenes. *Rheol. Acta* **1981**, *20*, 163–178. [[CrossRef](#)]

42. Li, D.; Xuan, X. Fluid rheological effects on particle migration in a straight rectangular microchannel. *Microfluid. Nanofluid.* **2018**, *22*, 49. [[CrossRef](#)]
43. Tirtaatmadja, V.; McKinley, G.H.; Cooper-White, J.J. Drop formation and breakup of low viscosity elastic fluids: Effects of molecular weight and concentration. *Phys. Fluids* **2006**, *18*, 043101. [[CrossRef](#)]
44. Dinic, J.; Biagioli, M.; Sharma, V. Pinch-off dynamics and extensional relaxation times of intrinsically semi-dilute polymer solutions characterized by dripping-onto-substrate rheometry. *J. Polym. Sci. Part B Polym. Phys.* **2017**, *55*, 1692–1704. [[CrossRef](#)]
45. Rubinstein, M.; Colby, R.H. *Polymer Physics*; Oxford University Press: Oxford, UK, 2003.
46. de Kort, D.W.; Rombouts, W.H.; Hoeben, F.J.M.; Janssen, H.M.; Van As, H.; van Duynhoven, J.P.M. Scaling Behavior of Dendritic Nanoparticle Mobility in Semidilute Polymer Solutions. *Macromolecules* **2015**, *48*, 7585–7591. [[CrossRef](#)]
47. de Gennes, P.-G. *Scaling Concepts in Polymer Physics*; Cornell University Press: Ithaca, NY, USA, 1979.
48. Xue, C.; Chen, X.; Liu, C.; Hu, G. Lateral migration of dual droplet trains in a double spiral microchannel. *Sci. China Phys. Mech.* **2016**, *59*. [[CrossRef](#)]
49. Liu, C.; Xue, C.; Chen, X.; Shan, L.; Tian, Y.; Hu, G. Size-Based Separation of Particles and Cells Utilizing Viscoelastic Effects in Straight Microchannels. *Anal. Chem.* **2015**, *87*, 6041–6048. [[CrossRef](#)]
50. Fu, T.; Wu, Y.; Ma, Y.; Li, H.Z. Droplet formation and breakup dynamics in microfluidic flow-focusing devices: From dripping to jetting. *Chem. Eng. Sci.* **2012**, *84*, 207–217. [[CrossRef](#)]
51. Deblais, A.; Velikov, K.P.; Bonn, D. Pearling Instabilities of a Viscoelastic Thread. *Phys. Rev. Lett.* **2018**, *120*, 194501. [[CrossRef](#)]
52. McKinley, G.H.; Sridhar, T. Filament-Stretching rheometry of complex fluids. *Annu. Rev. Fluid Mech.* **2002**, *34*, 375–415. [[CrossRef](#)]
53. Dinic, J.; Zhang, Y.; Jimenez, L.N.; Sharma, V. Extensional Relaxation Times of Dilute, Aqueous Polymer Solutions. *ACS Macro Lett.* **2015**, *4*, 804–808. [[CrossRef](#)]
54. Dinic, J.; Jimenez, L.N.; Sharma, V. Pinch-off dynamics and dripping-onto-substrate (DoS) rheometry of complex fluids. *Lab Chip* **2017**, *17*, 460–473. [[CrossRef](#)] [[PubMed](#)]
55. Hsiao, K.-W.; Sasmal, C.; Ravi Prakash, J.; Schroeder, C.M. Direct observation of DNA dynamics in semidilute solutions in extensional flow. *J. Rheol.* **2017**, *61*, 151–167. [[CrossRef](#)]
56. Stelter, M.; Brenn, G.; Yarin, A.; Singh, R.; Durst, F. Investigation of the elongational behavior of polymer solutions by means of an elongational rheometer. *J. Rheol.* **2002**, *46*, 507–527. [[CrossRef](#)]



© 2020 by the authors. Licensee MDPI, Basel, Switzerland. This article is an open access article distributed under the terms and conditions of the Creative Commons Attribution (CC BY) license (<http://creativecommons.org/licenses/by/4.0/>).